A hierarchical predictive control for supercapacitor-retrofitted grid-connected hybrid renewable systems

Mukalu Sandro Masaki, Lijun Zhang*, Xiaohua Xia

Department of Electrical, Electronic and Computer Engineering, University of Pretoria, Pretoria 0002, South Africa

Abstract

This paper presents a two-layer control strategy designed for easy integration of supercapacitors in a grid-integrated solar photovoltaic-battery hybrid renewable system, initially controlled by a typical model predictive control method. To operate the upgraded energy system, either without or with little modifications of the pre-existing architecture, an additional control layer is applied at the bottom of the original control system. Considering the complementary characteristics of batteries and supercapacitors, the design of the new model predictive control layer and its coordination with the original one help to deliver a stable power flow between the hybrid renewable system and the utility grid, and remove fast variations from the battery power. Actual measurements of solar radiation in South Africa are used to test the effectiveness of the proposed strategy. Simulations carried out on a 1-MW photovoltaic plant confirm the benefits in terms of adherence to power quality regulations, improved conditioning of the power generated by the intermittent renewable sources, and lifetime extension of the battery.

Keywords: Power smoothing, hybrid energy storage system, supercapacitor, model predictive control, renewable energy.

1. Introduction

For more than a decade, grid-integration of intermittent renewables such as wind turbines and solar photovoltaics (PVs) has proven to be an effective means to achieve progressive decarbonization of power systems [1, 2, 3]. However, the increasing penetration of weather-dependent generation poses risks to the reliability, stability, and economy of power supply [4, 5]. Among the proven solutions to this concern is the inclusion of energy storage systems (ESSs) such as a battery, flywheel, supercapacitor, superconducting magnetic energy storage, fuel-cell and pumped hydro [6, 7, 8].

Until recently, batteries were one of the most popular ESS due to their high energy density, flexibility and scalability [8, 9]. Accordingly, a multitude of control strategies for grid-integrated hybrid renewable systems (HRS) with a battery ESS were proposed in the literature. Besides the routine energy and power constraints applied to batteries, a few models were also presented to reduce wear of battery caused by the current flow. This includes minimizing a battery aging factor [10], penalizing the charge and discharge operations [11], keeping the state of health of batteries above a threshold [12], and implementing state of charge (SoC)-oriented control of the battery current [13]. The battery wear process can be hastened through fast/large variations of current flow that generate excessive heat and increase the internal resistance of the battery, causing further heating by the Joule's effect [14, 15, 16]. Presently, owners of grid-integrated renewable energy systems are being increasingly required by regulatory authorities to maintain a stable power profile at the point of common coupling (PCC) to the power grid [17, 18]. Therefore, despite the existence of wear control schemes, must handle the fluctuations introduced by intermittent renewable sources such as PV panels.

*Corresponding author. Tel: +27 (0) 12 420 2674.
Email address: lijun.zhang@up.ac.za (Lijun Zhang)

A cost-effective method to address the need for an EES that features fast response and long-term energy support is to combine two or more energy storage technologies into a hybrid ESS. Among the various possible options, the battery-supercapacitor (SC) association is presently preferred for power supply due to feasibility and maturity reasons [19, 20, 21, 22]. Batteries have a high energy density, but low power density and slow response speed. These characteristics are well balanced by the high power density, rapid response speed and low energy density of SCs. The power peak enhancement, internal losses reduction and lifetime extension achieved by a passive battery-SC hybrid ESS (energy storage devices directly mounted in parallel) were previously established under pulsed load [23] and pulsed charging sources [24]. However, in these works, the current sharing between the two energy storage devices is only determined by their internal voltages and internal resistances. The power flows of the battery and the SC cannot be controlled separately since their terminal voltages are forced to be equal at all times.

Various control strategies for power sharing between the energy storage components of a battery-SC ESS have been proposed in the literature. DC-bus voltage-based control schemes that use the battery to regulate the power balance in the DC grid and the SC to handle fast DC-bus voltage dynamics were presented in [25]. A model predictive controller (MPC) for battery-SC ESS that aims at supplying/absorbing the power allocated to the hybrid ESS, while directing the fast and slow current components to the SC and battery, respective, was proposed in [26]. Energy losses in the SC result in increased stress levels for the battery during power supply. An MPC scheme that minimizes the magnitude/fluctuation of the battery current and the energy loss seen in the SC was provided in [14]. A heuristic algorithm using a modified active parallel hybrid ESS, with SC-only connected through the DC/DC converter, was presented in [27]. In this strategy, the paths and directions of power flow within the battery-SC ESS are determined by a number of factors, including the power balance requirement, the terminal voltages of energy storage devices and the battery SoC. A variable two-stage rate-limit scheme for batteries was presented in [28]. Two different rate-limits are designed to optimize the charge/discharge rates and the amount of energy stored/released by the battery, taking the load requirement and the settling time into account. The SC is used to complement the battery during the transient period. Because only a few components of the energy system were involved in the design, these controllers achieve local energy management.

Control strategies that aim to coordinate the power flow across the entire renewable energy system have been proposed in the literature. A rule-based power management scheme for the dispatch of a PV power plant in compliance with the Australian grid regulation was proposed in [18]. An improved model, more robust against forecasting errors, was presented in [29]. A model predictive heuristic control that regulates the charge/discharge power of the battery was presented in [30]. In this study, wavelet theory is used to achieve a multi-layer decomposition of the power output of a wind generator. A control scheme with dynamic rate limiter designed for grid-connected wave energy park was provided in [31]. The dynamic rate limiter allows direct control over the magnitude of power variations of the battery. [32] proposed an energy management framework for a grid-integrated concentration photovoltaic plant. A second-order filter is developed for power allocation between the hybrid ESS components. A hierarchical dynamic optimal model for real-time tracking of the grid power reference was proposed in [33]. These strategies mainly focus on the control of utility-scale renewable plants, with little attention paid to the case of smaller systems, where the presence of local demand plays a significant role in the definition of operational objectives.

Among the previous research on this topic, a hierarchical energy management framework for multiple distributed PV-SC-load HRS with a centralized battery ESS was developed in [34]. First-order filters allow to allocate the high-frequency power components of the net power to the SC on site, while the low-frequency power components are direct to the centralized battery ESS. This ESS component also helps to maintain the power balance at the PCC. [35] proposed a heuristic designed to regulate the DC-bus voltage and smooth the power profile at the PCC. The power allocation between the ESS components is mainly determined by their SoC. A heuristic algorithm that regulates the DC-bus voltage, and the grid voltage and frequency, taking the grid availability and the electricity price into consideration, was presented in [36]. A heuristic algorithm that realizes the automatic selection of the operation mode of the battery among the pre-set modes was presented in [37]. While the SC is directly connected on the DC bus, the suitable operation mode, which depends on the direction and amplitude of the battery current, is chosen on the basis of the PV power

output, load demand and the battery SoC. A dynamic power sharing of excess and deficit powers between the grid and the EES components of a PV-based HRS be means of a heuristic algorithm was proposed in [38]. The power allocation considers the sign and magnitude of the net power, the SoC of the battery and the SC.

The main drawback of the various methods presented so far is that, in the case of pre-existing HRS equipped with batteries, a complete restructuring of the control system is required in order to implement the new controller for battery-SC ESS. This may raise concerns from plant owners with respect to technical (shut-down, decommissioning process), financial (decommissioning and disposal costs) and environmental (disposal of material) implications. In the literature, available to the authors, only a filtration-based control strategy for hybrid ESS retrofit in autonomous PV/battery domestic HRS was proposed in [39]. In this control model, the high-frequency components filtered from the measured battery current are used as the set-point for the SC, which absorbs from/feeds into the common bus through a DC-DC converter. Immediate benefits, particularly, decreased fluctuations in the battery current and reduction in battery health cost, were reported in this study. While the proposed solution can be also applied to grid-integrated PV-battery HRS, significant fluctuations remained in the battery current profile despite the presence of SC. The failure to account for the predictions of the battery current during the control of the SC can be cited among the reasons for this situation. Moreover, no control was conducted over the current flow and the energy level of the SC. Finally, by focusing on the battery alone, the SC provides no substantial advantage at the system level.

This paper presents a hierarchical predictive control of a grid-integrated PV/battery HRS retrofitted with SC. Under the existing system considered in this study, the control strategy presented in this paper has the following advantages: (1) no re-programming is required on the existing controller, since the SC is supervised by a new controller added in the control system; (2) reduces sudden variations in the power flow of the battery; (3) increased utilization rate of the renewable energy; (4) Stable power flow at the PCC; and (5) better tracking of the grid power reference.

2. Modelling of the grid-integrated hybrid power system

The HRS evaluated in this paper is illustrated in Figure 1, where the shaded area indicates the retrofitted equipment. It comprises solar PV panels, a battery bank, a supercapacitor bank and loads. Electric power can be absorbed from or fed into the utility grid at the PCC. Before the retrofit, the power management unit 1 (PMU-1) ensures the control of the solar PV and the battery via their respective DC-DC converters and the utility grid via an AC-DC inverter. A circuit breaker (CB) allows PMU-1 to connect and disconnect the power network. After the addition of the new equipment, the command signal of the PV and the grid is transferred to PMU-2, while the measurements are sent to both control units. Only the battery remains under control of PMU-1. Both PMUs are supplied with forecast data of the load demand and the PV generation. In practice, a single PMU, with sufficient computing power and memory resources, can play the role of PMU-1 and PMU-2. In that case, no modification is required to the architecture of the original control system.

In this study, we assume that the original HRS is controlled by an MPC scheme, designed for the purpose of either the minimization or the maximization of an objective. An example might be to increase the self-sufficiency and to encourage the use of solar energy, which implies minimizing the power consumption from the grid and maximizing the power supply by the PV system. In this context, because of both the relatively "large" control step (affecting the sampling rate of forecast data), necessary to prevent rapid variations of the battery power, and the limited degree of freedom offered by the HRS at this stage, little attention can be paid to the actual power quality at the PCC and the battery. The proposed retrofit with the SC aims to address this problem and to further increase the use of solar energy. The mathematical models of the HRS components are presented below.

2.1. Solar photovoltaic system

The solar PV system consists of solar arrays that harvest solar radiation and convert it into DC power. The solar radiation that strikes the surface of collectors of a solar panel has three components: direct-beam

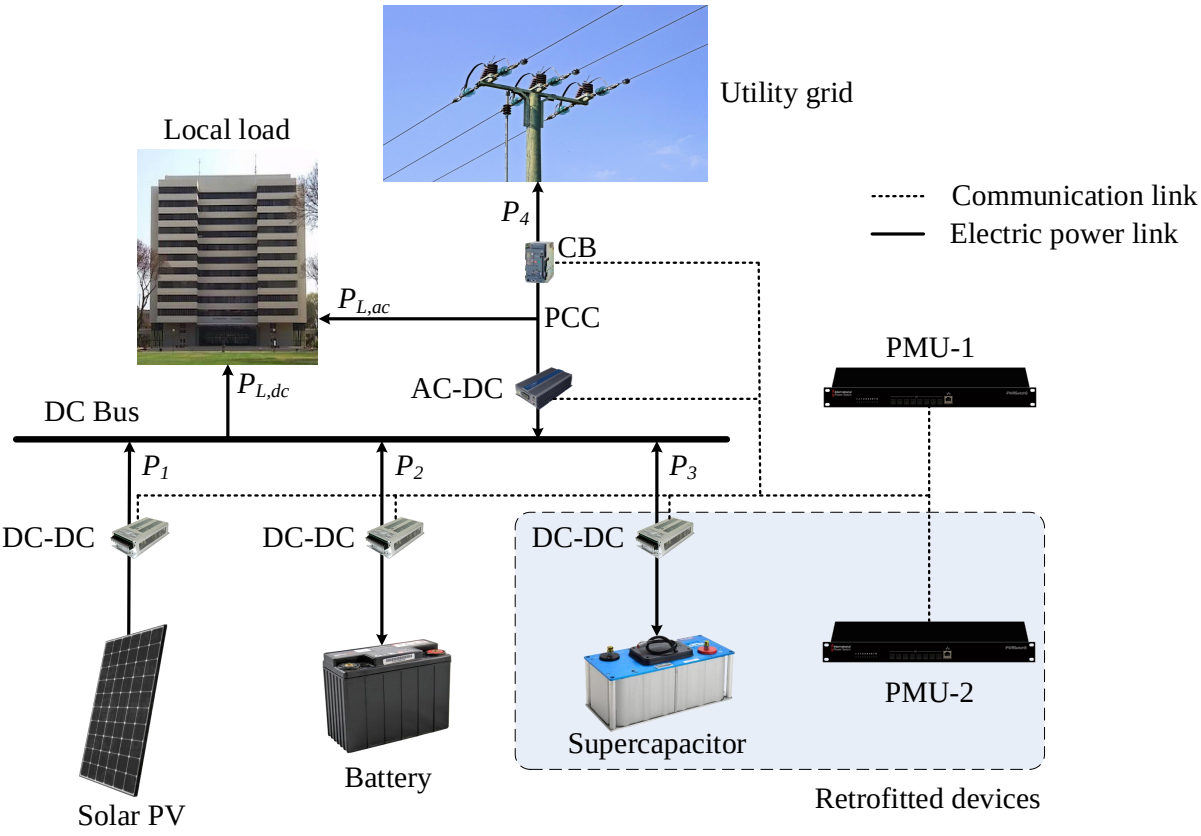

Figure 1: Layout of the grid-integrated HRS

radiation, diffuse radiation and reflected radiation.

The PV power output $P_{pv,BC}$ due to beam radiation $I_{BC}(k)$ that strikes the active surface of the PV panel at sample time k is given by [40]:

$$P_{pv,BC}(k) = \eta_{pv} I_{BC}(k) A_c, \tag{1}$$

where η_{pv} denotes the conversion efficiency of the solar panels, and A_c denotes the total active area of the panels. Beam radiation is translated from the direct-beam radiation $I_B(k)$ (normal to the rays) by

$$I_{BC}(k) = I_B(k) \cos\theta(k), \tag{2}$$

with the incident angle $\theta(k)$ given by

$$\cos\theta(k) = \cos\beta(k) \cos(\phi_S(k) - \phi_C(k)) \sin\psi + \sin\beta(k) \cos\psi. \tag{3}$$

In (3), $\beta(k)$ denotes the altitude angle, $\phi_S(k)$ denotes the solar azimuth angle, $\phi_C(k)$ denotes the azimuth angle of the panels, and ψ denotes the tilt angle of the PV panels as shown in Figure 2.

In the absence of actual measurements of diffused radiation, an estimation of the PV power output $P_{pv,DC}$ due to this component is given by [40]

$$P_{pv,DC}(k) = \eta_{pv} C I_B(k) \left(\frac{1 + \cos\psi}{2}\right) A_c, \tag{4}$$

with the sky diffuse coefficient C is approximated by [40]

$$C = 0.095 + 0.04 sin\left[\frac{360}{365}(n - 100)\right], \tag{5}$$

where n denotes the number of the day in the year.

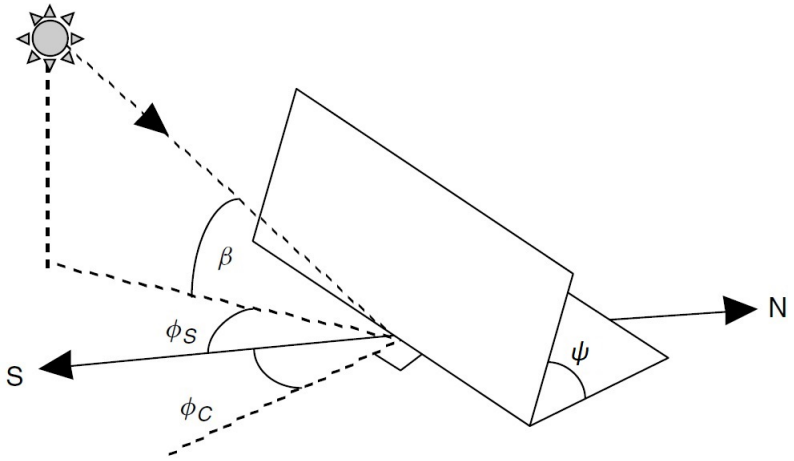

Figure 2: Collector azimuth angle $\phi_S(k)$, tilt angle ψ, solar azimuth angle $\phi_S(k)$ and altitude angle $\beta(k)$

In the absence of actual measurements of reflected radiation, an estimation of the PV power output $P_{pv,RC}(k)$ due to this component is given by [40]

$$P_{pv,RC}(k) = \eta_{pv}\rho I_B(k)\left(\sin\beta(k) + C\right)\left(\frac{1-\cos\psi}{2}\right)A_c, \tag{6}$$

where ρ denotes the ground reflectance.

The total power generation of the PV panel at sample time k, denoted by $P_{pv}(k)$, can be obtained by the summation of the components given in (1), (4) and (6):

$$P_{pv}(k) = P_{pv,BC}(k) + P_{pv,DC}(k) + P_{pv,RC}(k). \tag{7}$$

Depending on the operating conditions, the net power supply of the solar panels to the power system, denoted by P_1 in Figure 1, can vary between zero and the generated power

$$0 \leq P_1(k) \leq \eta_1 P_{pv}(k), \tag{8}$$

where η_1 denotes the efficiency of the DC-DC converter of the PV system. The excess portion of P_{pv} is dumped in a dissipative load (not shown in the Figure 1) whenever the set-point sent to the converter of the PV system is such as $P_{pv}(k) > P_1(k)/\eta_1$.

2.2. Battery bank

The battery power P_2 can be decomposed into charging power P_2^+ and discharging power P_2^-. The variation of the battery SoC induced by charging and discharging operations can be approximated by

$$SoC_b(k+1) = SoC_b(k) + \eta_2\eta_{b,c}P_2^+(k+1)\Delta T - \frac{1}{\eta_2\eta_{b,d}}P_2^-(k+1)\Delta T, \tag{9}$$

where $SoC_b(k+1)$ and $SoC_b(k)$ denote the battery SoC at, respectively, sample times $k+1$ and k, η_2 denotes the conversion efficiency of the DC-DC converter of the battery, $\eta_{b,c}$ and $\eta_{b,d}$ denote charging efficiency and discharging efficiency, respectively, and ΔT represents the sampling step. Based on (9), the battery SoC at sample time k is expressed as a function of the initial value $SoC_b(0)$ by

$$SoC_b(k) = SoC_b(0) + \eta_2\eta_{b,c}\sum_{\tau=0}^{k}P_2^+(\tau)\Delta T - \frac{1}{\eta_2\eta_{b,d}}\sum_{\tau=0}^{k}P_2^-(\tau)\Delta T, \tag{10}$$

At any sample time k, the battery SoC is subject to

$$\underline{SoC_b} \leq SoC_b(k) \leq \overline{SoC_b}, \tag{11}$$

where $\underline{SoC_b}$ and $\overline{SoC_b}$ are respectively the lower and upper bounds.

The battery must be operated so that the charging and discharging do not exceed their respective upper bound $\overline{P_{b,ch}}$ and $\overline{P_{b,disch}}$

$$0 \leq P_2^+(k) \leq \overline{P_{b,ch}}/\eta_2, \tag{12}$$

$$0 \leq P_2^-(k) \leq \eta_2 \overline{P_{b,disch}}. \tag{13}$$

The following constraint prevents simultaneous charging and discharging of batteries

$$P_2^+(k)P_2^-(k) = 0. \tag{14}$$

The resulting battery power P_2 is given by (15)

$$P_2(k) = P_2^-(k) - P_2^+(k). \tag{15}$$

2.3. Supercapacitors

The SC power P_3 can be decomposed into charging power P_3^+ and discharging power P_3^-. Similarly to the battery, the SC SoC at sample time k is expressed of in terms of the initial value $SoC_{sc}(0)$ by

$$SoC_{sc}(k) = SoC_{sc}(0) + \eta_3\eta_{sc,c}\sum_{\tau=0}^{k} P_3^+(\tau)\Delta T - \frac{1}{\eta_3\eta_{sc,d}}\sum_{\tau=0}^{k} P_3^-(\tau)\Delta T, \tag{16}$$

where $SoC_{sc}(k+1)$ and $SoC_{sc}(k)$ are the SC SoC at, respectively, sample times $k+1$ and k, η_3 denotes the conversion efficiency of the DC-DC converter of the SC, and $\eta_{sc,c}$ and $\eta_{sc,d}$ are, respectively, charging efficiency and discharging efficiency of the SC.

At any sample time k, the SC SoC is subject to

$$\underline{SoC_{sc}} \leq SoC_{sc}(k) \leq \overline{SoC_{sc}}, \tag{17}$$

where $\underline{SoC_{sc}}$ and $\overline{SoC_{sc}}$ denote, respectively, the lower and upper bounds.

The charging and discharging powers of the SC cannot exceed their respective upper bounds $\overline{P_{sc,ch}}$ and $\overline{P_{sc,disch}}$, and neither take place simultaneously

$$0 \leq P_3^+(k) \leq \overline{P_{sc,ch}}/\eta_3, \tag{18}$$

$$0 \leq P_3^-(k) \leq \eta_3\overline{P_{sc,disch}}, \tag{19}$$

$$P_3^+(k)P_3^-(k) = 0. \tag{20}$$

The resulting SC power P_3 is given by (21)

$$P_3(k) = P_3^-(k) - P_3^+(k). \tag{21}$$

2.4. Utility grid

The power flow P_4 between the HRS and the utility grid is composed of the power absorbed from the grid P_4^- and the power fed into to it P_4^+. The thermal capacity of the power link between the HRS and the grid, denoted by $\overline{P_{tie}}$, should not be exceeded at all times:

$$P_4^+(k) \leq \overline{P_{tie}}, \tag{22}$$

$$P_4^-(k) \leq \overline{P_{tie}}. \tag{23}$$

Simultaneous power consumption from and supply to the utility grid is also prevented by

$$P_4^+(k)P_4^-(k) = 0. \tag{24}$$

The resulting power exchange between the utility grid and the HRS is given by

$$P_4(k) = P_4^-(k) - P_4^+(k). \tag{25}$$

3. Model predictive controllers

In order to present the proposed retrofit control approach, an MPC strategy is assumed to be implemented on the existing grid-integrated HRS, which consists of PV panels, batteries, AC and DC loads. This MPC model is provided first. The design of the new control system is conducted afterwards.

3.1. MPC of grid-integrated PV-battery HRS

In this paper, the existing HRS is managed by an MPC strategy implemented on the control unit PMU-1 as shown Figure 1. In this context, the coordination of power flow across the HRS is performed for the purpose of either the maximization or the minimization of a performance index J that can be technical (e.g. energy autonomy), economic (e.g. operation cost), environmental (e.g. carbon footprint), social (e.g. comfort level), or a combination of these, and taking into consideration the various operation constraints (e.g. power balance, power and energy bounds). In this study, we assume that the control strategy aims to maximize both the self-sufficiency and the use of solar energy, which implies the minimization of the energy supplied by the utility grid and the minimization of the energy dumped in the dissipative load of the PV systems. To limit the thermal stress of the battery power, the sampling time ΔT is in the range of minutes.

In view of this and the system modeling detailed earlier, the discrete-time formulation of the MPC strategy for the existing HRS is as follows:

$$\min\ J(k) = \sum_{i=1}^{N_p} \Big[P_4^-(k+i) + \big(\eta_1 P_{pv}(k+i) - P_1(k+i)\big) \Big], \tag{26}$$

subject to

$$P_1(k+i) + P_2^-(k+i) - P_2^+(k+i) + \eta_4 P_4^-(k+i) - P_4^+(k+i)/\eta_4 = P_L(k+i), \tag{27a}$$

$$P_2^-(k+i) P_2^+(k+i) = 0, \tag{27b}$$

$$P_4^+(k+i) P_4^-(k+i) = 0, \tag{27c}$$

$$\underline{SoC_b} \le SoC_b(k) + \eta_2 \eta_{b,c} \sum_{\tau=k}^{k+i} P_2^+(\tau)\Delta T - \frac{1}{\eta_2 \eta_{b,d}} \sum_{\tau=k}^{k+i} P_2^-(\tau)\Delta T \le \overline{SoC_b}, \tag{27d}$$

$$0 \le P_1(k+i) \le \eta_1 P_{pv}(k+i), \tag{27e}$$

$$0 \le P_2^-(k+i) \le \eta_2 \overline{P_{b,disch}}, \tag{27f}$$

$$0 \le P_2^+(k+i) \le \overline{P_{b,ch}}/\eta_2, \tag{27g}$$

$$0 \le P_4^+(k+i) \le \overline{P_{tie}}, \tag{27h}$$

$$0 \le P_4^-(k+i) \le \overline{P_{tie}}, \tag{27i}$$

with $i = 1, \cdots, N_p$. Here, N_p denotes the prediction horizon, η_4 denotes efficiency of the inverter situated at the PCC, and the power demand $P_L(k+i)$ at time sample $k+i$ is given by

$$P_L(k+i) = P_{L,dc}(k+i) + P_{L,dc}(k+i)/\eta_4 \tag{28}$$

Due to the nonlinearity of (27b) and (27c), the optimization problem (26) and (27) is categorized as a nonlinear programming (NLP) to be solved at each sample time k.

3.2. Unified MPC of grid-integrated PV-battery-SC HRS

In this paper, the goals pursued by the addition of SC to the HRS are threefold: (1) to reduce the impact of the short-term fluctuations of solar energy and load demand upon the attainment of the operational objective expressed by the performance index; (2) to deliver a stable power profile at the PCC; (3) to prevent frequent variations of the battery power. At the control level, one approach to operate the upgraded HRS considering these goals and the SC characteristics is to replace the previous MPC strategy presented earlier by a new MPC strategy purposefully designed. In that case, a higher sampling rate of forecast data

and a shorter control step ΔT are necessary to allow the SC to play an effective role despite its limited energy capacity.

The proposed MPC strategy for grid-integrated PV-battery-SC HRS is indicated from (29) to (30p). Besides the update of the power balance in (30a) and the addition of constraints that control the power and energy flows of the SC ((30d), (30i), (30m) and (30n)), a few new constraints are also added to the previous MPC. Particularly, (30b) forces the grid power to remain constant over N_g consecutive control intervals. On the other hand, constraints (30f) and (30g) maintain the battery power between the ramp-rates limits $\underline{\Delta P_2}$ and $\overline{\Delta P_2}$.

$$\min J(k) = \sum_{i=1}^{N_p} \Big[P_4^-(k+i) + \big(\eta_1 P_{pv}(k+i) - P_1(k+i)\big) \Big], \tag{29}$$

subject to

$$P_1(k+i) + P_2^-(k+i) - P_2^+(k+i) + P_3^-(k+i) - P_3^+(k+i) + \eta_4 P_4^-(k+i) - P_4^+(k+i)/\eta_4 = P_L(k+i), \tag{30a}$$

$$P_4^+(k+s) = P_4^+(k+r), \tag{30b}$$

$$P_2^-(k+i)P_2^+(k+i) = 0, \tag{30c}$$

$$P_3^+(k+i)P_3^-(k+i) = 0, \tag{30d}$$

$$P_4^+(k+i)P_4^-(k+i) = 0, \tag{30e}$$

$$\underline{\Delta P_2} \le P_2^-(k+m) - P_2^-(k+n) \le \overline{\Delta P_2}, \tag{30f}$$

$$\underline{\Delta P_2} \le P_2^+(k+m) - P_2^+(k+n) \le \overline{\Delta P_2}, \tag{30g}$$

$$\underline{SoC_b} \le SoC_b(k) + \eta_2\eta_{b,c} \sum_{\tau=k}^{k+i} P_2^+(\tau)\Delta T - \frac{1}{\eta_2\eta_{b,d}} \sum_{\tau=k}^{k+i} P_2^-(\tau)\Delta T \le \overline{SoC_b}, \tag{30h}$$

$$\underline{SoC_{sc}} \le SoC_{sc}(k) + \eta_3\eta_{sc,c} \sum_{\tau=k}^{k+i} P_3^+(\tau)\Delta T - \frac{1}{\eta_3\eta_{sc,d}} \sum_{\tau=k}^{k+i} P_3^-(\tau)\Delta T \le \overline{SoC_{sc}}, \tag{30i}$$

$$0 \le P_1(k+i) \le \eta_1 P_{pv}(k+i), \tag{30j}$$

$$0 \le P_2^-(k+i) \le \overline{P_{b,ch}}/\eta_2, \tag{30k}$$

$$0 \le P_2^+(k+i) \le \eta_2 \overline{P_{b,disch}}, \tag{30l}$$

$$0 \le P_3^-(k+i) \le \eta_3 \overline{P_{sc,disch}}, \tag{30m}$$

$$0 \le P_3^+(k+i) \le \overline{P_{sc,ch}}/\eta_3, \tag{30n}$$

$$0 \le P_4^+(k+i) \le \overline{P_{tie}}, \tag{30o}$$

$$0 \le P_4^-(k+i) \le \overline{P_{tie}}, \tag{30p}$$

with $i = 1, \cdots, N_p$, $m = n+1, \cdots, n+N_b-1$, $n = 0, N_b, 2N_b, \cdots, N_p - N_b$, $s = r+1, \cdots, r+N_g-1$, and $r = 0, N_g, 2N_g, \cdots, N_p - N_g$.

When compared with the MPC strategy implemented on the existing HRS in Section 3.1, the above MPC ensures a longer service life for the batteries and a better power profile at the PCC. However, because of the long prediction horizon N_p required for energy management reasons (in the range of 24 hours or more), the relatively short control step ΔT required for power quality reasons (in the range of tens of seconds), and the nature and size of the new MPC strategy, the indicated benefits can be achieved only at the expense of significant increase in computing power and memory resources to allow the implementation of such a controller. A less resource-intensive alternative to this control approach is provided in the next Section.

3.3. Hierarchical MPC of grid-integrated PV-battery-SC system

3.3.1. Architecture and design

Figure 3 shows the general architecture of the proposed two-layer control framework. Using the MPC of the existing PV-battery HRS as the upper layer, a second MPC strategy implemented in the control

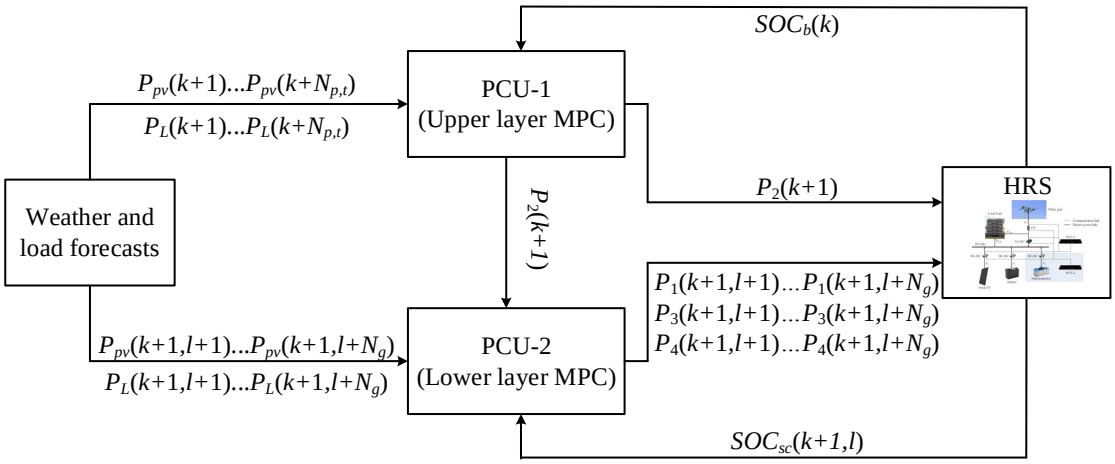

Figure 3: Control architecture of the hierarchical MPC strategy

unit PMU-2 (see Figure 1) operates at the bottom layer to achieve a finer control. As mentioned earlier, a single PMU with sufficient resources can be used to execute the two controllers, thus avoiding a partial modification of the original control architecture.

The MPC at the upper layer is used the same way as before the addition of the SC (see 3.1), with the only difference being that the optimal control sequences obtained for the PV and the grid are discarded. As shown in Figure 3, the first element $P_2(k+1)$ in the optimal sequence of the battery is used to control the device and is passed on to PMU-2 for further optimization at the bottom layer. As indicated earlier, the prediction horizon of the existing MPC is in the range of 24 hours or more to account for the cycles of solar energy and local demand. Moreover, a sampling step in the range of minutes is applied to extend the service life of the battery. Accordingly, the MPC executed at the upper layer is provided in Section 3.3.2, and is derived from that of the existing HRS in Section 3.1.

At the bottom layer stage, the next upper layer control step $k+1$ is divided into even subintervals in the lower control layer, as shown in Figure 3. At the time instant $(k+1,l)$, which marks the end of the current subinterval, the SC SoC, the power set-point $P_2(k+1)$ of the battery, and short-term forecast data of solar energy and load demand are used as input to the MPC at the bottom layer. The short-term forecast data supplied to PMU-2 are in the range of minutes, with a sampling rate in the order of seconds. While keeping P_2 as provided by the upper layer helps address the thermal stress of the battery, relevant constraints are included in the bottom layer MPC to deliver a smooth power profile at the PCC, as detailed in Section 3.3.3. Upon completion of the computation process, the first N_g elements of the control sequences of P_1, P_3 and P_4 computed at the bottom layer controller are sent to the power conditioning units for implementation.

3.3.2. Upper layer MPC model

Since this control strategy is directly inherited from the existing HRS, Eqs. (31) to (32i) is taken from Section 3.1. Let the t subscript denote the upper layer variables, the MPC implemented at the upper layer ca be formulated as follows

$$\min J_t(k) = \sum_{i=1}^{N_{p,t}} \Big[P_{4,t}^{-}(k+i) + \big(\eta_1 P_{pv,t}(k+i) - P_{1,t}(k+i)\big) \Big], \tag{31}$$

s.t.

$$P_{1,t}(k+i)+P_{2,t}^{-}(k+i)-P_{2,t}^{+}(k+i)+\eta_4 P_{4,t}^{-}(k+i)-P_{4,t}^{+}(k+i)/\eta_4=P_{L,t}(k+i), \tag{32a}$$

$$P_{2,t}^{+}(k+i)P_{2,t}^{-}(k+i)=0, \tag{32b}$$

$$P_{4,t}^{+}(k+i)P_{4,t}^{-}(k+i)=0, \tag{32c}$$

$$\underline{SoC_b}\le SoC_b(k)+\eta_2\eta_{b,c}\sum_{\tau=k}^{k+i}P_2^{+}(\tau)\Delta T_t-\frac{1}{\eta_2\eta_{b,d}}\sum_{\tau=k}^{k+i}P_2^{-}(\tau)\Delta T_t\le\overline{SoC_b}, \tag{32d}$$

$$0\le P_{1,t}(k+i)\le\eta_1 P_{pv,t}(k+i), \tag{32e}$$

$$0\le P_{2,t}^{+}(k+i)\le\overline{P_{b,ch}}/\eta_2, \tag{32f}$$

$$0\le P_{2,t}^{-}(k+i)\le\eta_2\overline{P_{b,disch}}, \tag{32g}$$

$$0\le P_{4,t}^{+}(k+i)\le\overline{P_{tie}}, \tag{32h}$$

$$0\le P_{4,t}^{-}(k+i)\le\overline{P_{tie}}, \tag{32i}$$

with $i=1,\cdots,N_{p,t}$.

3.3.3. Lower layer MPC model

Let the b subscript denote the lower layer variables, the MPC implemented at the bottom layer can be formulated as follows

$$\min J_b(k,l)=\sum_{j=1}^{N_{p,b}}\Big[P_{4,b}^{-}(k+i)+\big(\eta_1 P_{pv,b}(k+i)-P_{1,b}(k+i)\big)\Big], \tag{33}$$

s.t.

$$\begin{aligned}&P_{1,b}(k,l+j)+P_{2,t}^{-}(k,l+j)-P_{2,t}^{+}(k,l+j)+P_{3,b}^{-}(k,l+j)-P_{3,b}^{+}(k,l+j)+\\&\eta_4 P_{4,b}^{-}(k,l+j)-P_{4,b}^{+}(k,l+j)/\eta_4=P_{L,b}(k,l+j),\end{aligned} \tag{34a}$$

$$P_{4,b}^{+}(k,l+r)=P_{4,b}^{+}(k,l+s), \tag{34b}$$

$$P_{3,b}^{+}(k,l+j)P_{3,b}^{-}(k,l+j)=0, \tag{34c}$$

$$P_{4,t}^{+}(k,l+j)P_{4,t}^{-}(k,l+j)=0, \tag{34d}$$

$$\underline{SoC_{sc}}\le SoC_{sc}(k,l)+\eta_3\eta_{sc,c}\sum_{\tau=l}^{l+i}P_3^{+}(k,\tau)\Delta T_b-\frac{1}{\eta_3\eta_{sc,d}}\sum_{\tau=l}^{l+i}P_3^{-}(k,\tau)\Delta T_b\le\overline{SoC_{sc}}, \tag{34e}$$

$$0\le P_{1,b}(k,l+j)\le\eta_1 P_{pv,b}(k,l+j), \tag{34f}$$

$$0\le P_{3,b}^{+}(k,l+j)\le\overline{P_{sc,ch}}/\eta_3, \tag{34g}$$

$$0\le P_{3,b}^{-}(k,l+j)\le\eta_3\overline{P_{sc,disch}}, \tag{34h}$$

$$0\le P_{4,b}^{+}(k,l+j)\le\overline{P_{tie}}, \tag{34i}$$

$$0\le P_{4,b}^{-}(k,l+j)\le\overline{P_{tie}}, \tag{34j}$$

with $l=1,N_g{+}1,2N_g{+}1,\cdots,(M{-}1)N_g{+}1$, $M=\Delta T_t/(\Delta T_b N_g)$, $j=0,\cdots,N_{h,b}{-}1$, $r=0,N_g,2N_g,\cdots,N_{h,b}{-}N_g$, and $s=r+1,r+2,\cdots,r+N_g-1$. As before, N_g denotes the number of control steps over which the grid power should be kept constant. The algorithm 1 summarizes the operation of the hierarchical control strategy.

4. Case Study

Considering the load profile shown in Figure 4(a) and the grid connection of the HRS [40], a 1-MW solar PV is considered to test and compare the control strategies presented in this study. Historical measurements of the direct and diffuse solar radiations are collected from the solar radiometric station at the University

Algorithm 1 Hierarchical Model Predictive Control

For time k, minimize (31) subject to (32)
for $m = 0$ to $M - 1$ **do**
    Set $l = mN_g + 1$
    Minimize (33) subject to (34)
    for $n = 0$ to $N_g - 1$ **do**
        Implement $P_{1,b}(k, l+n)$, $P^{+}_{2,t}(k)$, $P^{+}_{2,t}(k)$, $P^{+}_{3,b}(k, l+n)$, $P^{-}_{3,b}(k, l+n)$, $P^{+}_{4,b}(k, l+n)$, $P^{-}_{4,b}(k, l+n)$
    End for
End for

of Pretoria (25° 45' S and 28° 13.72' E)[41, 42]. The solar radiation data are applied to the PV arrays oriented South-North and tilted at 36°. The PV power output due to reflected radiation is estimated using Eq. (6), and the contributions due to direct-beam and diffused radiations are determined by Eqs. (1) and (4), respectively. The conversion efficiency of solar panels is provided in Table 1.

The prediction horizon and the control horizon are set at 24 hours and 30 minutes, respectively, at the upper layer, and 30 minutes and five minutes, respectively, at the bottom layer. The sampling times are respectively set at 30 minutes and 10 seconds. The solar radiation during a sampling interval of the upper layer is set equal to the average of actual measurements sampled at a one-minute interval. The presumed impact of the forecast errors and the difference of sampling rates between the upper layer (one minute) and the lower layer (ten seconds) is mimicked by adding a white Gaussian noise to the actual solar radiation data, with a signal-to-noise ratio (SNR) of 25dB. Similarly, the load profile at the bottom layer (sampled at 5-minute intervals) is derived from that of the upper layer (sampled at 30-minute intervals) by the addition of a white Gaussian noise, with a SNR of 35dB. When compared to the solar radiation, a higher SNR is applied to the load since, at a facility level, the fluctuations of the load are usually less deep than those of the solar radiation, which is directly affected by the movement of clouds.

The energy storage system consists of a 250-kW/1464-kWh bank of lead-acid batteries [43] and a 13.1-MW/5.74-kWh bank of electrostatic double-layer capacitors (supercapacitors) [44]. The rest of the simulation parameters are provided in Table 1.

5. Simulation and discussion

A PC Core(TM) i5, 3.00 GHz, with 8 GB of RAM running Windows 10, was used to simulate the control strategies presented in this paper. Classified as nonlinear programmings (NLPs), the optimization problems were solved in MATLAB using the "fmincon" function. Because of the limited resources of the PC, the short sampling period (10 seconds) and the long prediction horizon (24 hours), the unified MPC of grid-integrated HRS provided in Section 3.2 takes far too long to simulate and is therefore impractical for real-time applications. Consequently, the discussion is limited to comparing the MPC of PV-battery HRS and the hierarchical MPC of PV-battery-SC HRS. Moreover, because the former is identical in all respects to the upper layer of the latter, we discuss the performances of the upper layer against those of the full hierarchical MPC.

5.1. MPC of grid integrated PV-battery power system (Upper layer)

Figure 4(a) shows the forecasted load profile $P_{L,t}$, the forecasted PV generation $P_{pv,t}$ and the resulting PV power supply $P_{1,t}$ and grid power $P_{4,t}$. The power and SoC of the battery are shown in Figure 4(b). It is observed that during night hours and before sunrise, the utility grid covers most of the energy needs in the HRS, while the remaining part is locally supplied by the battery until the minimum SoC is reached. During daylight hours, the power generated by the solar PV is primarily used to supply the load and charge the battery. Only excess power is fed into the utility grid.

A superimposition of the PV generation based on forecast during the upper layer and the bottom layer is shown in Figure 5(a), and that of the load demand is shown in Figure 5(b). To maintain the power system balanced, the excess and deficit induced by the fluctuations of the PV generation and the load

Table 1: Parameters of the hybrid renewable system

Parameter	Value	Unit
Solar PV		
η_{pv}	0.124	
ρ	0.20	
Battery bank		
$\eta_{b,c}$	0.85	
$\eta_{b,d}$	1	
$\overline{P_{b,ch}}$ & $\overline{P_{b,disch}}$	250	kW
$\overline{SoC_b}$	0.9	p.u
$\underline{SoC_b}$	0.50	p.u
Supercapacitors		
$\eta_{sc,c}$	0.80	
$\eta_{sc,d}$	1	
$\overline{P_{sc,ch}}$ & $\overline{P_{sc,disch}}$	4 857	kW
$\overline{SoC_{sc}}$	1	p.u
$\underline{SoC_{sc}}$	0.25	p.u
Utility grid		
$\overline{P_{tie}}$	1 200	kW
DC-DC converters		
η_1	0.90	
η_2, η_3	0.85	
AC-DC inverter		
η_4	0.95	

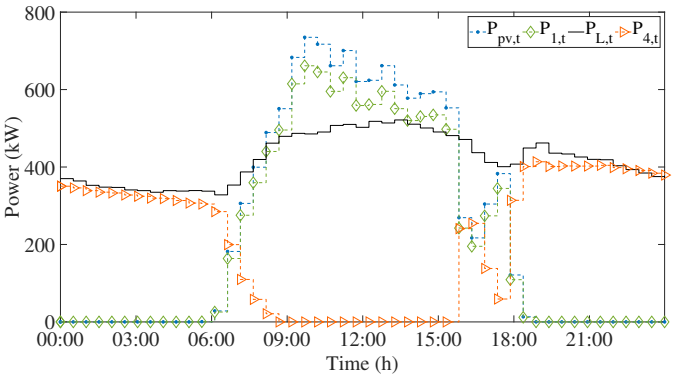

(a) Load demand and power profiles of the PV and the grid

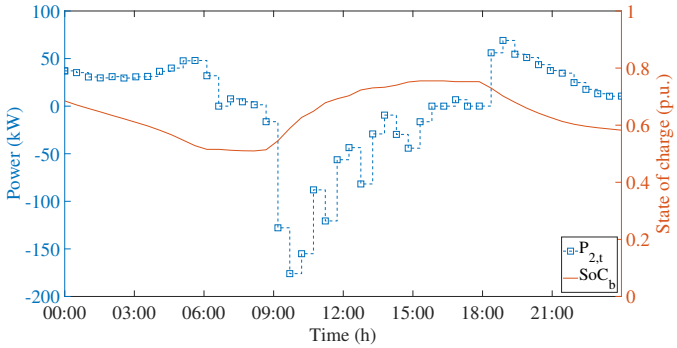

(b) Power and SoC of the battery

Figure 4: Demand profile and control inputs of original MPC strategy (upper layer)

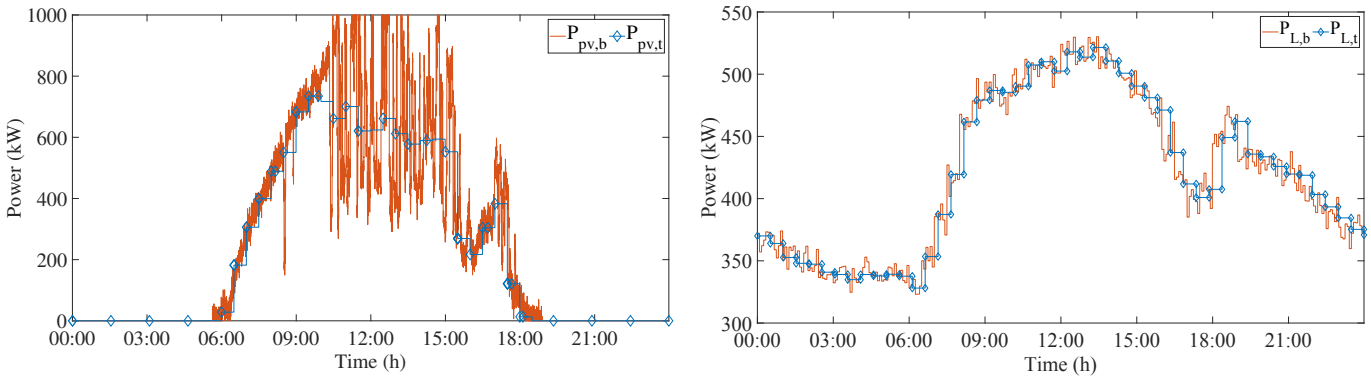

(a) PV generation

(b) Load profile

Figure 5: Upper vs. bottom layer predictions of the PV generation and the load demand

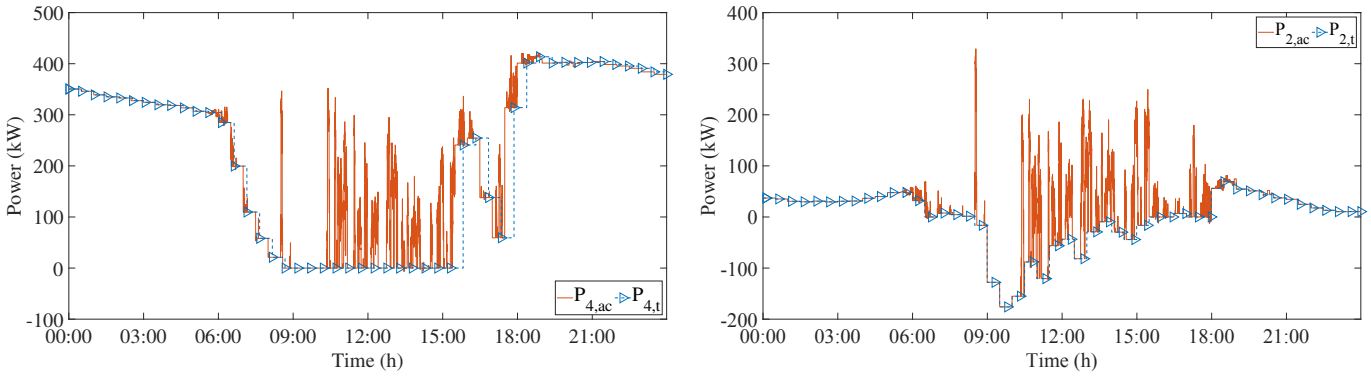

(a) Power flow at the PCC

(b) Power flow of the battery

Figure 6: Optimized vs. actual power flows at the PCC and the battery

demand should be handled either by the grid or the battery. The resulting power profiles at the PCC and the battery are presented in Figure 6(a) and Figure 6(b), respectively. In Figure 6(a), $P_{4,ac}$ denotes the actual power profile at the PCC when the fluctuations are handled by the utility grid alone. Similarly, $P_{2,ac}$ denotes the actual battery power when this device handles the fluctuations alone. It is worth reminding that any excess power from the PV is dumped to the dissipative load connected to the PV system. Figure 6 shows that, unless appropriate actions are taken, the large peaks observed may pose a risk either to the safety of the network system (frequency stability) or the safety and lifetime of the battery (overheating).

5.2. Hierarchical MPC of grid integrated PV-battery-SC system

Figure 7 presents the power profile at the PCC before and after the implementation of the bottom layer. The new layer proves to be effective in both regulating the power exchanged with the power network and conditioning the PV generation to maximize its supply to the HRS. The increase observed in the amount of renewable energy fed into the grid contributes to creating eco-friendly networks for little extra investment.

The comparison between the battery power and the SC power in Figure 8(a) shows that the fluctuations are fully handled by the SC so that the battery power is perfectly stable. Figure 8(b) shows that, like the battery, the SC get discharged after sunset as a result of an attempt to reduce the power consumption from the utility grid.

5.3. Comparison of power and energy performances

A quantitative comparison between the existing control strategy and the proposed one can be carried out using the performance indicators shown in Table 2. Here, the second and third columns correspond to the existing MPC before and after considering the impact of the fluctuations, respectively. The last column corresponds to the hierarchical MPC control strategy. It is worth mentioning that the losses in the

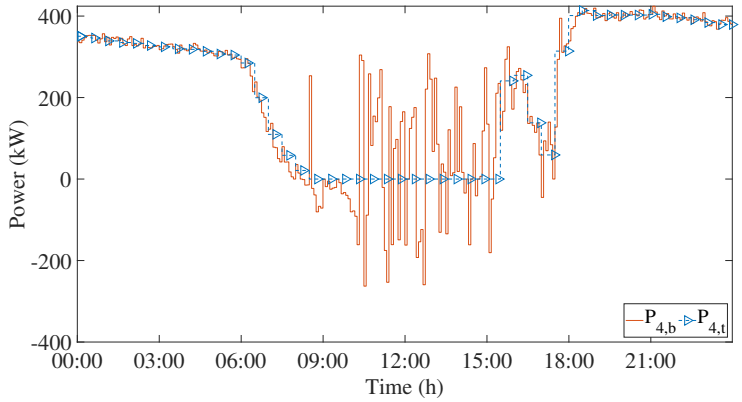

Figure 7: Power flow at the PCC: MPC PV-battery vs. Hierarchical MPC PV-batt-SC

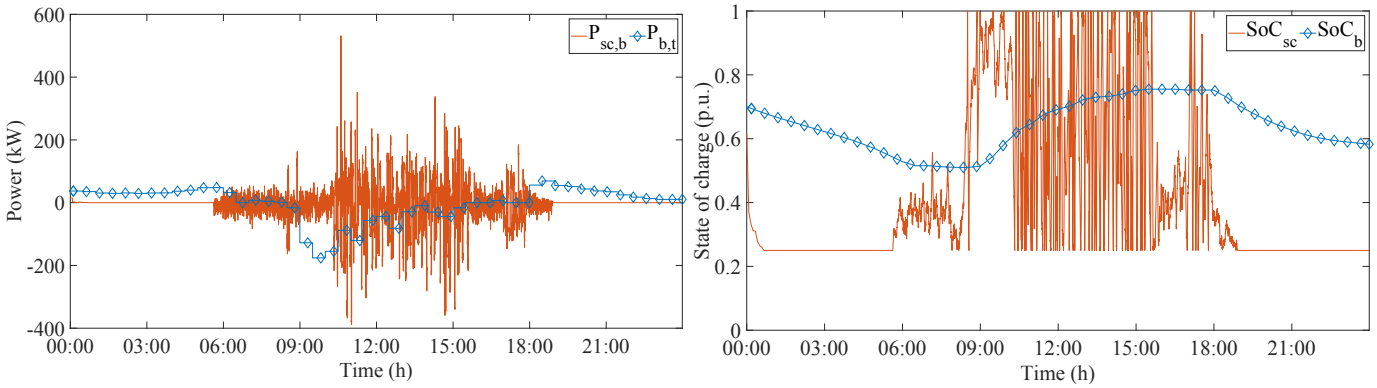

(a) Power flow comparison

(b) SoC comparison

Figure 8: Comparison of power and SoC profiles of the ESS components

Table 2: Comparison between existing MPC and hierarchical MPC

Performance indicator	MPC (optimized)	MPC (actual)	Hierarchical MPC
PV energy generation (kWh)	5796.93	6153.18	6153.18
PV energy supply (kWh)	5217.24	4866.26	5348.00
PV energy dissipated (%)	0.00	12.13	3.41
Total energy import (kWh)	5187.26	5540.97[1]	5594.46
Total energy export (kWh)	0.00	14.86[1]	313.47
5-min intervals with stable P_4 (%)	100	66.67[1]	100
$max(\lvert P_2 + P_3 \rvert)$ (kW)	176.00	329.08[1]	509.03

[1] Fluctuations handled by the utility grid

Table 3: Duration of the lower layer prediction horizon vs energy performances

Predic. horiz.	Avg time[1]	Max. time[1]	PV supply[2]	Grid import[2]	Grid export[2]
5 min.	0.09	0.88	5301.84	5668.60	331.42
10 min.	0.42	9.39	5349.00	5594.46	313.47
15 min.	1.09	31.17	5380.64	5591.11	347.50
20 min.	3.45	125.07	5388.33	5591.42	352.72
30 min.	8.68	237.88	5387.80	5590.56	351.83

[1] in seconds; [2] in kWh

DC-DC converter of the PV contribute, with the dumping load, to the difference between the PV energy generation and the PV energy supply. Comparing the first two columns Table 2, it shows that failing to handle the fluctuations of PV power and load demand prevents the HRS to benefit from the increase in PV generation over the implementation stage. With regard to the use of the energy generated by the PV system, a smaller part of it is effectively supplied to the HRS, while an increased quantity (+12.13%) is dumped in the dissipative load. Moreover, an increase in energy consumption from the grid without a significant counterpart is also noticed. Depending on which system component provides support for power balance in this condition, the frequency stability of the network system or the health of the battery may be jeopardized.

Comparing the last two columns in Table 2, a net increase in the use of solar energy is observed, with only 3.08% wasted in the dissipative load. Despite the operation of the SC leads to a direct increase in energy absorbed from the utility grid (+53.49 kWh), a net diminution (-245.12 kWh) is finally achieved thanks to the additional electricity fed into it. Moreover, the hierarchical control ensures the stability of the power profile at the PCC. The hybrid ESS also provides greater power support to the HRS without further involvement of the battery.

5.4. Setting of the duration of the prediction horizon at the bottom layer

Table 3 presents the average and maximum computation times and the selected energy indicators as functions of the length of the prediction horizon at the bottom layer. In general, long prediction horizons lead to better energy performances than short ones, i.e., increase in energy supply by the solar PV, decrease in consumption from the utility grid, and increase in energy fed into it can be observed. However, this is achieved at the cost of extra computation time, which negatively affects the implementability of the optimal control sequences. Accordingly, a trade-off is necessary between the energy benefit and the extra computation time incurred. In that regard, Table 3 shows that ten-minute prediction horizon leads to energy performances fairly close to those of longer duration, with an acceptable timing in average. However, five-minute prediction horizon might be preferred, since the computation time under the ten-minute prediction horizon can reach up to 9 seconds.

6. Conclusion

This paper has presented a hierarchical model predictive strategy designed to facilitate the addition of supercapacitors to a pre-existing grid-integrated hybrid renewable system equipped with batteries, initially

controlled by a typical model predictive controller. By means of a second control layer, this control strategy uses the supercapacitor to deliver a stable power profile at the point of common coupling. Moreover, the variable components of the power requested from the hybrid energy storage system are fully handled by the supercapacitor, so that the battery power remains stable. Simulations carried out on a practical case study have shown the validity and effectiveness of the proposed control strategy. Opportunities in terms of adherence to power quality regulations, improved conditioning of the power generated by the intermittent renewable sources, and lifetime extension of the battery have been also established.

References

[1] M. Haller, S. Ludig, N. Bauer, Decarbonization scenarios for the eu and mena power system: Considering spatial distribution and short term dynamics of renewable generation, Energy Policy 47 (2012) 282–290.

[2] M. Fripp, Switch: a planning tool for power systems with large shares of intermittent renewable energy, Environmental science & technology 46 (11) (2012) 6371–6378.

[3] M. Winskel, N. Markusson, B. Moran, G. Taylor, Decarbonising the UK energy system: accelerated development of low carbon energy supply technologies, Available: http://www.ukerc.ac.uk/publications/decarbonising-the-uk-energy-system-accelerated-development-of-low-carbon-energy-supply-technologies.html (Accessed: Aug. 01, 2018).

[4] E. K. Hart, E. D. Stoutenburg, M. Z. Jacobson, The potential of intermittent renewables to meet electric power demand: current methods and emerging analytical techniques, Proceedings of the IEEE 100 (2) (2012) 322–334.

[5] L. Bird, M. Milligan, D. Lew, Integrating variable renewable energy: Challenges and solutions, Tech. rep., National Renewable Energy Laboratory (NREL), Golden, CO. (2013).

[6] H. Tazvinga, X. Xia, J. Zhang, Minimum cost solution of photovoltaic–diesel–battery hybrid power systems for remote consumers, Solar Energy 96 (2013) 292–299.

[7] F. Wamalwa, S. Sichilalu, X. Xia, Optimal control of conventional hydropower plant retrofitted with a cascaded pumpback system powered by an on-site hydrokinetic system, Energy Conversion and Management 132 (2017) 438–451.

[8] T. Bocklisch, Hybrid energy storage systems for renewable energy applications, Energy Procedia 73 (2015) 103–111.

[9] G. L. Soloveichik, Battery technologies for large-scale stationary energy storage, Annual review of chemical and biomolecular engineering 2 (2011) 503–527.

[10] Z. Wu, H. Tazvinga, X. Xia, Demand side management of photovoltaic-battery hybrid system, Applied Energy 148 (2015) 294–304.

[11] B. Zhu, H. Tazvinga, X. Xia, Switched model predictive control for energy dispatching of a photovoltaic-diesel-battery hybrid power system, IEEE Transactions on Control Systems Technology 23 (3) (2015) 1229–1236.

[12] Y. Riffonneau, S. Bacha, F. Barruel, S. Ploix, et al., Optimal power flow management for grid connected pv systems with batteries, IEEE Transactions on Sustainable Energy 2 (3) (2011) 309–320.

[13] J. Hu, Y. Xu, K. W. Cheng, J. M. Guerrero, A model predictive control strategy of pv-battery microgrid under variable power generations and load conditions, Applied Energy 221 (2018) 195–203.

[14] M.-E. Choi, S.-W. Kim, S.-W. Seo, Energy management optimization in a battery/supercapacitor hybrid energy storage system, IEEE Transactions on Smart Grid 3 (1) (2012) 463–472.

[15] D. Linden, Handbok of Batteries, McGraw-Hill, 1994.

[16] S. Pay, Y. Baghzouz, Effectiveness of battery-supercapacitor combination in electric vehicles, in: Power Tech Conference Proceedings, 2003 IEEE Bologna, Vol. 3, IEEE, 2003, pp. 6–pp.

[17] National Energy Regulator of South Africa, Grid connection code for renewable power plants (RPPs) connected to the electricity transmission system (TS) or the distribution system (DS) in South Africa (July 2016), Available: http://www.nersa.org.za/Admin/Document/Editor/file/Electricity/TechnicalStandards/Newable%20Energy/SAGC%20Requirements%20for%20Renewable%20Power%20Plants%20Rev%202%209.pdf (Accessed: Aug. 01, 2018).

[18] G. Wang, M. Ciobotaru, V. G. Agelidis, Power smoothing of large solar pv plant using hybrid energy storage, IEEE Transactions on Sustainable Energy 5 (3) (2014) 834–842.

[19] L. Feng, J. Zhang, G. Li, B. Zhang, Cost reduction of a hybrid energy storage system considering correlation between wind and pv power, Protection and Control of Modern Power Systems 1 (1) (2016) 11.

[20] J. Li, Y. Xue, L. Tian, X. Yuan, Research on optimal configuration strategy of energy storage capacity in grid-connected microgrid, Protection and Control of Modern Power Systems 2 (1) (2017) 35.

[21] M. Ding, B. Wang, Z. Chen, Z. Chen, Y. Luo, G. Zheng, Stabilizing control strategy of complementary energy storage in renewable energy system, in: Innovative Smart Grid Technologies-Asia (ISGT Asia), 2012 IEEE, IEEE, 2012, pp. 1–5.

[22] W. Zuo, R. Li, C. Zhou, Y. Li, J. Xia, J. Liu, Battery-supercapacitor hybrid devices: Recent progress and future prospects, Advanced Science 4 (7) (2017) 1600539.

[23] R. A. Dougal, S. Liu, R. E. White, Power and life extension of battery-ultracapacitor hybrids, IEEE Transactions on Components and Packaging Technologies 25 (1) (2002) 120–131.

[24] T. Ma, H. Yang, L. Lu, Development of hybrid battery–supercapacitor energy storage for remote area renewable energy systems, Applied Energy 153 (2015) 56–62.

[25] N. R. Tummuru, M. K. Mishra, S. Srinivas, Dynamic energy management of hybrid energy storage system with high-gain pv converter, IEEE Transactions on Energy Conversion 30 (1) (2015) 150–160.

[26] B. Hredzak, V. G. Agelidis, M. Jang, A model predictive control system for a hybrid battery-ultracapacitor power source, IEEE Transactions on Power Electronics 29 (3) (2014) 1469–1479.
[27] C. Xiang, Y. Wang, S. Hu, W. Wang, A new topology and control strategy for a hybrid battery-ultracapacitor energy storage system, Energies 7 (5) (2014) 2874–2896.
[28] S. K. Kollimalla, A. Ukil, H. Gooi, U. Manandhar, N. R. Tummuru, Optimization of charge/discharge rates of a battery using a two-stage rate-limit control, IEEE Transactions on Sustainable Energy 8 (2) (2017) 516–529.
[29] G. Wang, M. Ciobotaru, V. G. Agelidis, Power management for improved dispatch of utility-scale pv plants, IEEE Transactions on Power Systems 31 (3) (2016) 2297–2306.
[30] X. Han, F. Chen, X. Cui, Y. Li, X. Li, A power smoothing control strategy and optimized allocation of battery capacity based on hybrid storage energy technology, Energies 5 (5) (2012) 1593–1612.
[31] A. Parwal, M. Fregelius, I. Temiz, M. Göteman, J. G. de Oliveira, C. Boström, M. Leijon, Energy management for a grid-connected wave energy park through a hybrid energy storage system, Applied Energy 231 (2018) 399–411.
[32] P. Roncero-Sánchez, A. Parreño Torres, J. Vázquez, Control scheme of a concentration photovoltaic plant with a hybrid energy storage system connected to the grid, Energies 11 (2) (2018) 301.
[33] M. S. Masaki, L. Zhang, X. Xia, Hierarchical power flow control of a grid-tied photovoltaic plant using a battery-supercapacitor energy storage system, Energy Procedia 145 (2018) 32–37.
[34] C. Ye, S. Miao, Q. Lei, Y. Li, Dynamic energy management of hybrid energy storage systems with a hierarchical structure, Energies 9 (6) (2016) 395.
[35] N. R. Tummuru, M. K. Mishra, S. Srinivas, Dynamic energy management of renewable grid integrated hybrid energy storage system, IEEE Transactions on Industrial Electronics 62 (12) (2015) 7728–7737.
[36] S. Kotra, M. K. Mishra, A supervisory power management system for a hybrid microgrid with hess, IEEE Transactions on Industrial Electronics 64 (5) (2017) 3640–3649.
[37] A. Aktas, K. Erhan, S. Özdemir, E. Özdemir, Dynamic energy management for photovoltaic power system including hybrid energy storage in smart grid applications, Energy 162 (2018) 72–82.
[38] U. Manandhar, A. Ukil, G. H. Beng, N. R. Tummuru, S. K. Kollimalla, B. Wang, K. Chaudhari, Energy management and control for grid connected hybrid energy storage system under different operating modes, IEEE Transactions on Smart Griddoi:10.1109/TSG.2017.2773643.
[39] W. Jing, D. K. Ling, C. H. Lai, W. S. Wong, M. D. Wong, Hybrid energy storage retrofit for standalone photovoltaic-battery residential energy system, in: Innovative Smart Grid Technologies-Asia (ISGT-Asia), 2017 IEEE, IEEE, 2017, pp. 1–6.
[40] G. M. Masters, Renewable and Efficient Electric Power Systems, John Wiley & Sons, 2013.
[41] M. Brooks, S. du Clou, J. van Niekerk, P. Gauche, C. Leonard, M. Mouzouris, A. Meyer, N. van der Westhuizen, E. van Dyk, F. Vorster, Sauran: A new resource for solar radiometric data in southern africa, Journal of Energy in Southern Africa 26 (2015) 2–10.
[42] Southern African Universities Radiometric Network, University of Pretoria - Hatfield Campus metering station [Online], Available: http://sauran.net/ShowStation.aspx?station=5 (Feb. 06, 2017).
[43] Current Automation, Sealed and vented lead-acid batteries [Online], Available: http://www.rectifier.co.za/Catalogue/hoppecke.pdf (Accessed: Apr. 01, 2017).
[44] Maxwell ® Technologies, Supercapacitor datasheet [Online], Available: http://www.maxwell.com/products/ultracapacitors/downloads (Accessed: Apr. 01, 2017).